

Article

Morpho-tectonic Assessment of the Abu-Dabbab Area, Eastern Desert, Egypt: Insights from Remote Sensing and Geospatial Analysis

Abdelrahman Khalifa ^{1,*} , Bashar Bashir ² , Abdullah Alsalman ² and Nazik Öğretmen ³ 

¹ Department of Geology, Faculty of Science, Al-Azhar University, Cairo 11651, Egypt

² Department of Civil Engineering, College of Engineering, King Saud University, Riyadh 11421, Saudi Arabia; bbashir@ksu.edu.sa (B.B.); alsalman@ksu.edu.sa (A.A.)

³ Climate Geochemistry Department, Max Planck Institute for Chemistry, 55128 Mainz, Germany; n.ogretmen@mpic.de

* Correspondence: akhalifa@azhar.edu.eg

Abstract: The Abu-Dabbab area, located in the central part of the Egyptian Eastern Desert, is an active seismic region where micro-earthquakes ($\approx M_L < 2.0$) are recorded regularly. Earthquake epicenters are concentrated along an ENE–WSW trending pattern. In this study, we used morphological indexes, including the valley floor width-to-valley floor height ratio (V_f), mountain front sinuosity (S_{mf}), the asymmetry factor index (A_f), the drainage basin shape index (B_s), the stream length–gradient index (S_L), hypsometric integral (H_i) water drainage systems, and a digital elevation model analysis, to identify the role of tectonics. These indexes were used to define the relative tectonic activity index (RTAI), which can be utilized to distinguish low (RTAI < 1.26), moderate (RTAI = 1.26–1.73), and high (RTAI > 1.73) tectonic activity signals all over the study area. Firstly, our results indicate low to medium tectonic activity and general anomaly patterns detected along the major tectonic zones of the study area. Secondly, based on most of the low to medium tectonic activity distributed in the study area and the detected anomalies, we discuss two potential drivers of the seismicity in the Abu-Dabbab area, which are fault-controlled and deep-rooted activities.

Keywords: morphological indexes; remote sensing; active tectonics; geospatial analysis; Abu-Dabbab; Egypt



Citation: Khalifa, A.; Bashir, B.; Alsalman, A.; Öğretmen, N. Morpho-tectonic Assessment of the Abu-Dabbab Area, Eastern Desert, Egypt: Insights from Remote Sensing and Geospatial Analysis. *ISPRS Int. J. Geo-Inf.* **2021**, *10*, 784. <https://doi.org/10.3390/ijgi10110784>

Academic Editor: Peter Blišťan

Received: 16 August 2021

Accepted: 12 November 2021

Published: 17 November 2021

Publisher's Note: MDPI stays neutral with regard to jurisdictional claims in published maps and institutional affiliations.



Copyright: © 2021 by the authors. Licensee MDPI, Basel, Switzerland. This article is an open access article distributed under the terms and conditions of the Creative Commons Attribution (CC BY) license (<https://creativecommons.org/licenses/by/4.0/>).

1. Introduction

Examining active tectonic features plays a significant role in understanding how landforms are formed and developed. For example, mountain fronts form as a result of tectonic and erosional processes [1,2], plateaus are formed as a result of mantle driven uplift, such as the Central Anatolian Plateau in Turkey [3] and the Colorado Plateau in the United States [4], and graben basins are formed by active normal faulting, such as in the Northern Apennines in Italy [5]. Usually, tectonically active regions undergo a significant risk of natural hazards, and using advanced science and technology may help in mitigating these potential hazards. In the last decade, tectonic geomorphology, remote sensing, and geospatial analysis have become efficient tools to identify the active tectonic spots, uplift and incision rates, slip rates on active faults, and present-day tectonic activity [6–13]. Assessment of the morphological indexes in regions of tectonic activity is a very efficient exercise to obtain extensive clues to investigate active tectonics and trigger mechanisms (e.g., faulting or mantle upwelling). Through quantitative analysis of data recovered via geospatial and remote sensing techniques, these indexes can be utilized to identify the distribution of the different tectonic signals. Tectonic signal refers to any cue reflected in the geomorphology by tectonic activities. For example, the mountain front sinuosity index can be erosional or tectonic (i.e., fault-controlled). The latter, in

this case, can be considered as a tectonic signal and can be derived through quantitative geomorphology analysis [11,14]. Morphological anomalies are abnormal morphological structures that can be detected by comparing these results with computed tectonic activity degrees. This method is very advantageous in examining the Abu-Dabbab seismic area, where there have been no sufficient studies on tectonics and morphology. Accordingly, studying geomorphic indexes in addition to extracting the lineaments from satellite images (e.g., Landsat 8 and ASTER images) over catchments, rivers, and streams using the remote sensing and GIS techniques allows us to distinguish between active and inactive landforms such as faults and catchments [15–20]. Quantitative assessment of the drainage networks, therefore, provides important information to investigate the recent deformation and its trigger mechanisms.

The Abu-Dabbab area is located at the western flank of the Red Sea and constitutes the intersection of the Nubian and Arabian plates [21–24]. The Red Sea was formed as an ocean spreading center when the Arabian Plate diverged from the African Plate during the Early Miocene [25]. The study area represents part of the Red Sea Mountain Chain, which includes the backbone of rugged and high mountains that are parallel to the Red Sea coastline [26,27]. In this study, two major valleys (*wadis*, in local language) that drain into the Abu-Dabbab region have been examined—Wadi Abu-Dabbab and Wadi Mubarak (Figure 1). Economically, the area was highlighted by the mining industry because it includes some gold mines in addition to many valuable minerals, such as feldspar, quartz, and phosphate [27].

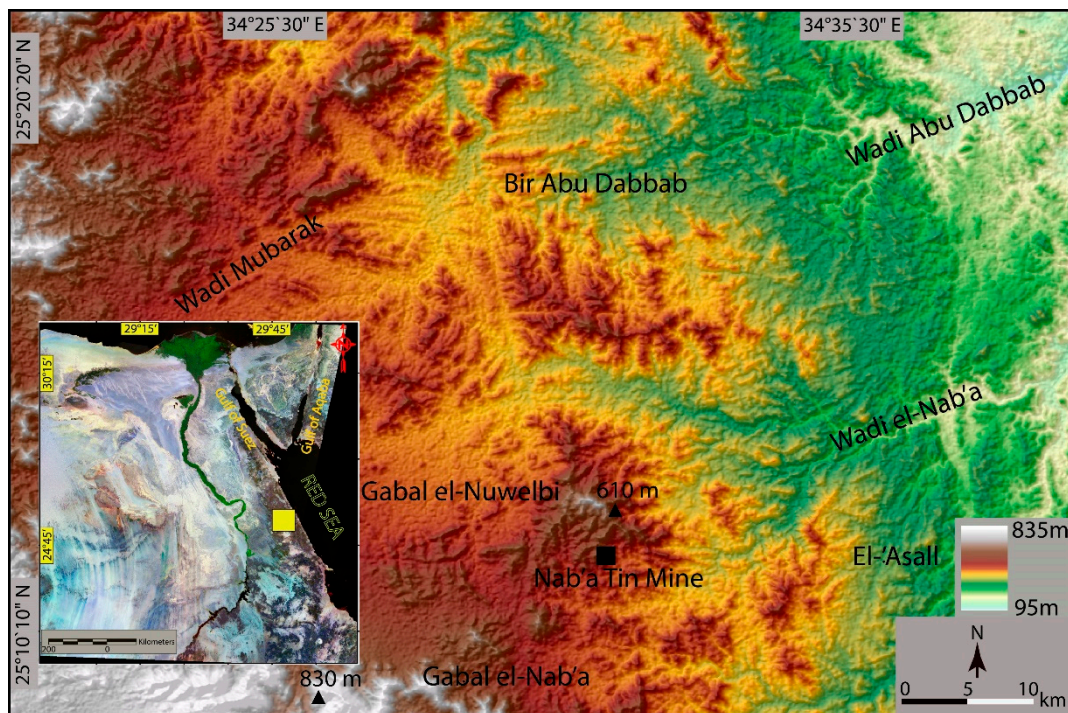


Figure 1. Shaded relief image illustrates the main features of the study area. The yellow square shows the location of the study area. Digital elevation model (DEM) data of the study area was downloaded from the USGS EarthExplorer (<https://earthexplorer.usgs.gov/>, accessed on 10 November 2021).

Together with its economic importance, the Abu-Dabbab area has a long history of earthquakes that have attracted many researchers to investigate its seismic activity and earthquake swarms [28–31]. The source of the seismicity of the Abu-Dabbab area has been widely discussed based on the two contrasting opinions of tectonic and/or deep-root (mantle) origin [26,27]. Many researchers have proposed that the influence of regional tectonics is the main source of the high-degree tectonic activities for long periods in the Abu-Dabbab area [26,32–34]. They have stated that the central Eastern Desert fault system

affects the study area greatly and reflects a structural heterogeneity in the upper crust of the Abu-Dabbab area. Accordingly, the upper crust is currently affected by an ongoing brittle deformation [26]. On the contrary, some authors have suggested that the heterogeneity in structural zones was initiated by the under-crust magmatic activity or the upper-crust fluids [22,35]. They have concluded that the study area was affected by different stress fields—local stresses because of the magmatic flow beneath the crust or regional stress orientations related to the Red Sea rift system. A geodynamic model was interpreted by the author in Ref. [31], explaining that in the Abu-Dabbab area, there are linear seismic regions, including active faults under a large Precambrian Igneous block.

In different regions, the concept of mantle-triggered uplift and related seismicity has been commonly applied, and the topographical response of such regions in terms of geomorphological properties has been investigated [36–40]. In this present study, we examined various morphological indexes using geospatial analysis and derived a regional relative tectonic activity index (RTAI) to decipher and evaluate the tectonic activity of the Abu-Dabbab area. Subsequently, we aimed to enhance our understanding of the driving factors of the region's landscape development and the origin of seismicity in this region for the first time.

2. Geological Setting

The Abu-Dabbab area is bounded by longitudes 34.35° to 34.65° E and latitudes 25.15° to 25.35° N (Figure 1). It occupies a region of about 640 km² at the south-eastern part of the Egyptian Eastern Desert. The Abu-Dabbab area is located far north of Marsa Alam city and west of the Red Sea coast by 30 and 29 km, respectively (Figure 1). The Abu-Dabbab area represents a part of the central Eastern Desert that mostly consists of low-grade volcano-sedimentary rocks with large gabbroic and granitic intrusion [41] (Figure 2). The oldest units in the region are metasediments that are composed of alternating beds of metasandstone, meta-greywackes, and quartzite-feldspar paraschist [26,41]. The study area comprises a small intrusion of talk-carbonate serpentines and gabbro rock units. The intruded bodies are mostly dissected by strike-slip and normal faults. The granitic rocks of the Abu-Dabbab area were divided into two major rock types—older and younger granites [41,42]. Tectonically, two sides of the Red Sea are affected by a major NW–SE tectonic trend in addition to the sinistral Najd Fault Shear Zone (NFSZ), which crosses both the Red Sea and the Arabian–Nubian Shield for about 1000 km [43]. The author in Ref. [44] classified the main tectonic elements in the Eastern Desert into three categories—(i) E–W trending fault systems, (ii) the Gulf of Suez trending fault systems, and (iii) the Gulf of Aqaba trending fault systems. Some researchers consider the Abu-Dabbab area a big, dome-like structure [27]. The study area is characterized by several elongated rock units, such as ophiolitic metagabbro and intrusive metagabbro to metadiorite, that are dissected by various fractures (Figure 2). Three different structural lineaments are distributed over the whole area in different directions. In the study area, the strike-slip faults are NNW–SSE trending, whereas normal faults are N–S trending (Figure 2).

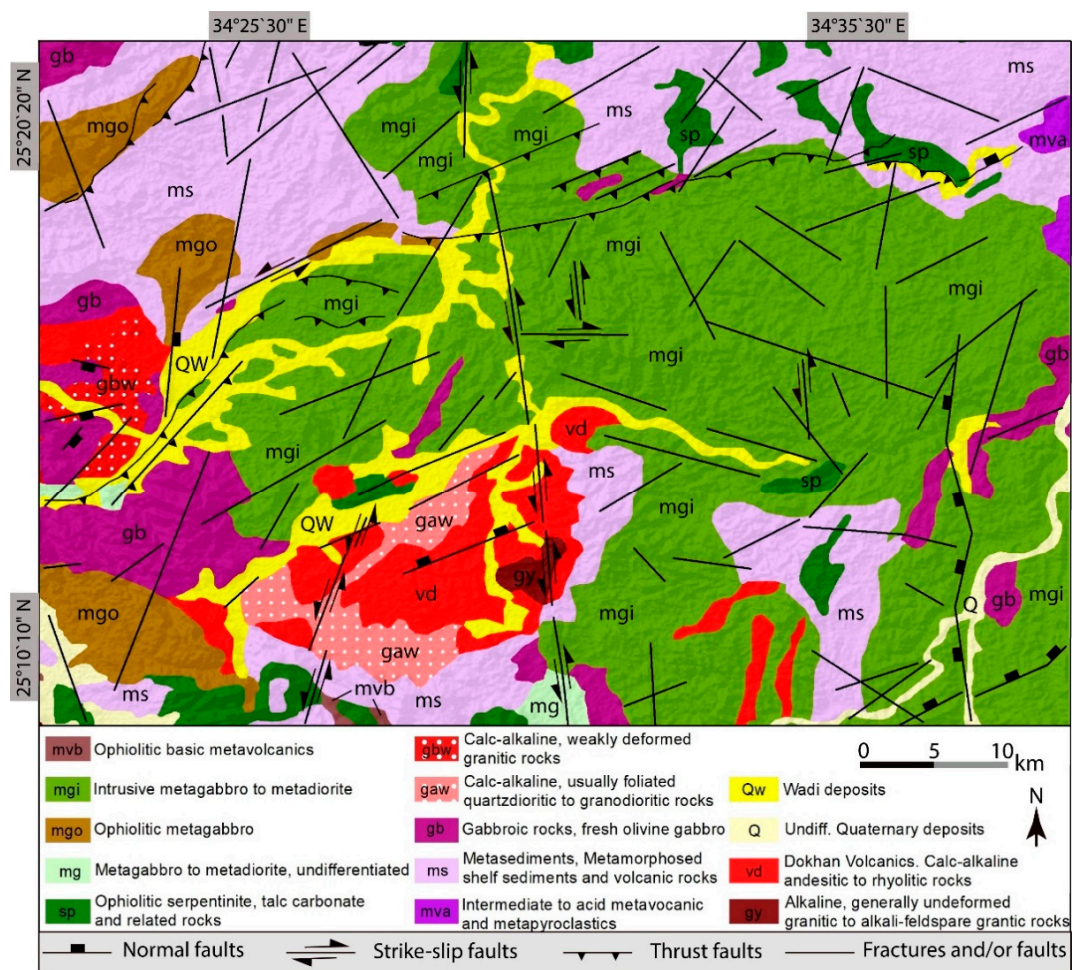


Figure 2. Geological map of the study area, modified after [26,45].

3. Seismicity

The first record of seismicity at the Abu-Dabbab area was measured instrumentally after 1970. The first micro-earthquake swarms were reported by Ref. [32]. The local Bedouins (travelers) in this region described this event by a huge sound similar to a quarry blast sound [46,47]. As they continued to hear this sound, the Bedouins named the area "Abu-Dabbab" which translates to "father of heavy loud knocking" in the local language. The micro-earthquake epicenters are distributed along the ENE–WSW direction within a tectonically active zone, which transverses the Red Sea Mountains (Figure 3) [26]. Two seismic events, on 12 November 1955, and 2 July 1984, with earthquake magnitudes of 5.5 and 5.1, respectively, are the latest seismic activities that have occurred in the last 100 years in this region [27]. Most of the seismicity focal depths in the Abu-Dabbab area are recorded at a range of 2 to 16–17 km [27].

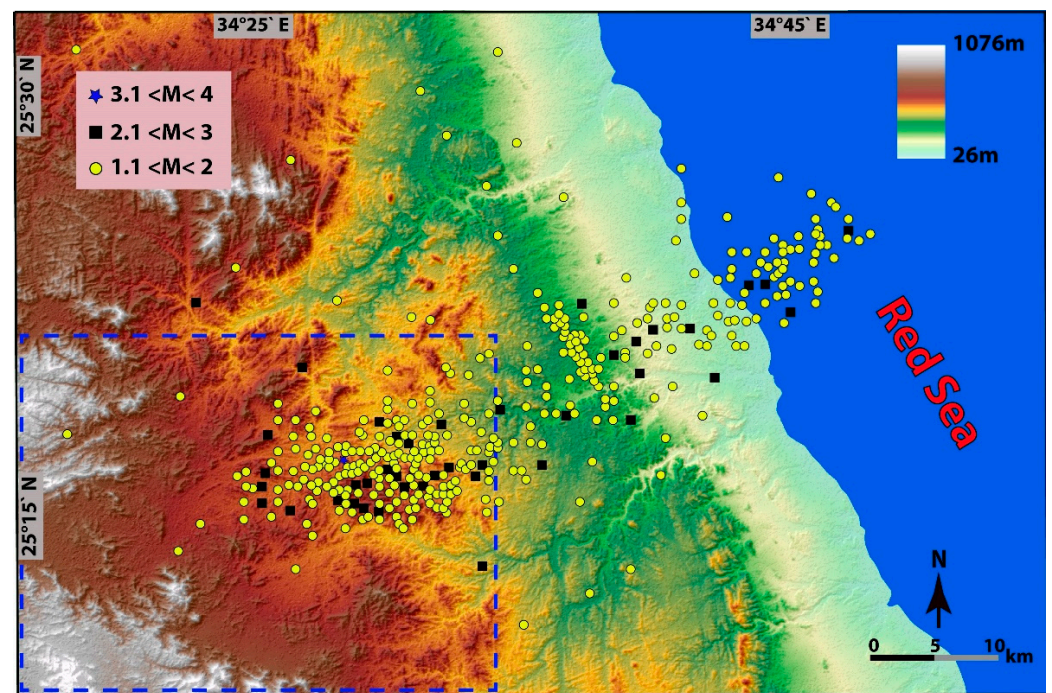


Figure 3. Seismicity map of the study area and surroundings showing earthquakes between October 2008 and April 2010, modified after [48]. Blue dashed rectangle shows the study area.

4. Methodology

4.1. Remote Sensing

Advanced Spaceborne Thermal Emission and Reflection Radiometer (ASTER) and Landsat-8 (OLI) imagery were used to produce greyscale base images utilizing ENVI 5.0 software. Image processing, such as contrast stretching and edge detection, was applied to enhance the greyscale image quality. PCI Geomatica software was utilized to process the greyscale images to extract different lineaments. The produced lineaments were compared with previous studies [43,44] that have reported on the geological features to identify the coinciding tectonic elements. Some linear structures, such as railroads and rivers, were carefully removed from our dataset. The Abu-Dabbab area lacks studies that focus on its tectonic framework. Therefore, it has required extensive fieldwork to map the various unknown tectonic elements. Based on the previously reported data [26,41,45], lineaments were categorized into normal faults, strike-slip faults, thrust faults, and fractures and/or faults.

4.2. Morphological Indexes

An ASTER digital elevation model (DEM) with a spatial resolution of 30 m was generated for the study area. ArcGIS 10.4 software was utilized to produce the greyscale hillshade image to detect different tectonic features. Drainage networks and watersheds were visualized from the ASTER-DEM data utilizing the data management and spatial analyst tools (hydrology functions) (Figure 4a,b). We followed the classification of Ref. [49]. The study area was classified into 74 sub-catchments (Figure 4b). Various morphological indexes were identified and computed from the ASTER-DEM and Google Earth Pro engine. Morphological indexes are calculated from either mountain fronts or drainage sub-catchments to identify differing tectonic activities, such as local scale uplift and subsidence [1,2,7,10].

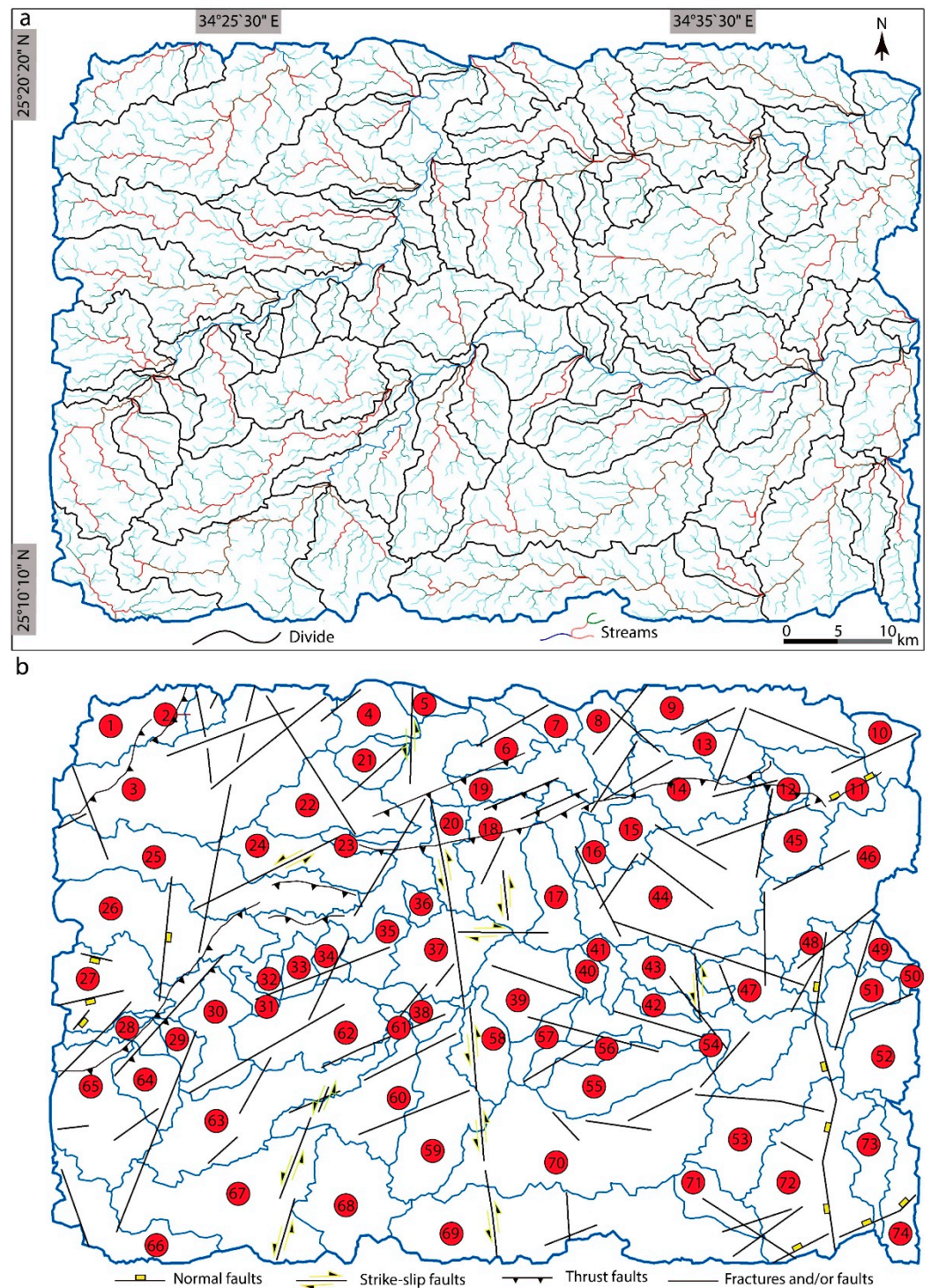


Figure 4. (a) Drainage and sub-catchments extracted from ASTER-DEM data. (b) Map showing the reference numbers of the sub-catchments and the tectonic features of the study area.

4.2.1. Valley Floor Width-to-Valley Floor Height Ratio (V_f)

V_f index describes the uplifting and valley base level galling. It is a very effective index to detect the valley shape and action of valley incision [50]. This parameter is applied by the following equation:

$$V_f = 2V_{fw} / [(E_{ld} - E_{sc}) + (E_{rd} - E_{sc})] \quad (1)$$

where V_{fw} represents the width of the valley floor, E_{ld} and E_{rd} are the measures of the right and left valley elevations, respectively, and finally, E_{sc} is the average elevation of the valley floor [49].

4.2.2. Mountain Front Sinuosity (S_{mf})

The mountain front sinuosity index (S_{mf}) is an effective parameter for evaluating the tectonic activity levels along mountain fronts [50,51]. The S_{mf} is calculated using the following equation:

$$S_{mf} = L_{mf}/L_s \quad (2)$$

where L_{mf} is the sinuous length of the mountain front, and L_s is the straight-line length of the mountain front.

4.2.3. Asymmetry Factor Index (A_F)

The A_F index is the calculation of separate catchments to estimate the asymmetry degree of catchments and evaluate the tectonic activity level [50]. This index is applied through the following equation:

$$A_F = (A_r/A_t) \times 100 \quad (3)$$

where A_r is the total area of the catchment to the right of the main catchment trunk, while A_t is the total area of the catchment.

4.2.4. Drainage Basin Shape Index (B_s)

Young catchments reflect a high degree of tectonic activity with elongated shapes that tend to cover tectonically active regions. Active elongated catchments turn into catchments with circular shapes as the tectonic activity is reduced with time [49,52]. This index is calculated as follows:

$$B_s = B_i/B_w \quad (4)$$

where B_i is the length of a catchment from the headwaters to the mouth, and B_w is the distance between the two walls of the catchments at the widest part of the catchment.

4.2.5. Stream Length–Gradient Index (S_L)

The stream length–gradient index is calculated to examine the change in stream course and slope affected by tectonic and lithological (i.e., rock strength type) units. The S_L index is calculated using the following equation [53]:

$$S_L = (\Delta H/\Delta L) \times L \quad (5)$$

where $\Delta H/\Delta L$ represents the channel slope of the catchment reach mean catchment, and L is the distance between the reach midpoint and the watershed divide.

However, when examining the lithological units of the study area (Figure 2), we found that most of the lithology reflects the same rock strength type; hence, the S_L parameter was neglected and the other morphological indexes were averaged to map the spatial distribution of the RTAI in the study area.

4.2.6. Hypsometric Integral (H_i)

The H_i index is a very effective tool to illustrate the distribution of elevation of a specific landscape, particularly a drainage catchment [39]. This index helps to calculate the volume of a catchment that has not undergone any erosion actions. The authors in Refs. [50,54] have expressed a simple formula to calculate this index as follows:

$$H_i = \text{Elev}_{\text{mean}} - \text{Elev}_{\text{min}}/\text{Elev}_{\text{max}} - \text{Elev}_{\text{mean}} \quad (6)$$

where $Elev_{mean}$ is the mean catchment elevation, $Elev_{max}$ is the maximum catchment elevation, and $Elev_{min}$ is the minimum catchment elevation.

4.3. Relative Tectonic Activity Index (RTAI)

In this study, the relative tectonic activity index (RTAI) method was applied separately along the 74 sub-catchments. The average values of five computed indexes were estimated to yield the RTAI and to help illustrate the distribution of the relative active tectonics of the study area [55]. For the RTAI evaluation, we divided the morphological indexes into tectonic activity classes, as high (Class 1), moderate (Class 2), and low (Class 3) tectonic activity.

5. Results

5.1. Valley Floor Width-to-Valley Floor Height Ratio (V_f)

The V_f values were calculated for 74 sub-catchments in the study area. The calculated data were extracted across the mainstream for every sub-catchment. The V_f values were grouped into high, medium, and low tectonic activity classes (Figure 5a,b). The locations of the calculated V_f index are shown in Figure 5a, and the V_f values of the Abu-Dabbab area are shown in Figure 5b. The values of this index are range from 0.11 to 0.15 for Sub-catchments 2 and 4, respectively, and the highest value $V_f = 5$ was computed for Sub-catchment 68. Generally, most of the sub-catchments had low V_f values, while the highest values covered a large area in the south part of the study area (Figure 5b). Accordingly, tectonic classes of the Sub-catchments 37 and 22, as inferred from the V_f values, were Class 1 and Class 2, respectively. The low tectonic V_f class was recorded for the remaining 15 sub-catchments.

5.2. Mountain Front Sinuosity (S_{mf})

The results of the S_{mf} index vary from 0.73 to 2.26 along the studied mountain fronts of every tectonic segment (Table 1). While the lowest value was calculated for the strike-slip fault segment 16, the highest value was computed for the fault and/or fracture segment 40 (Table 1, Figure 6).

Table 1. Values and classes of S_{mf} for 107 identified mountain front segments.

Mountain Front Segments	Catchments	S_{mf}	Class	Mountain Front Segments	Catchments	S_{mf}	Class
NFs1	10, 11	1.11	Class 1	Fr/Fs55	29, 63, 64, 67	1.19	Class 1
NFs2	48, 51	1.61	Class 2	Fr/Fs56	-	-	-
NFs3	53, 72	1.17	Class 1	Fr/Fs57	65	1.32	Class 1
NFs4	72	1.09	Class 1	Fr/Fs58	66	1.39	Class 1
NFs5	72	1.01	Class 1	Fr/Fs59	63	1.88	Class 2
NFs6	72, 37, 74	1.01	Class 1	Fr/Fs60	62, 63	1.86	Class 2
NFs7	72	1.17	Class 1	Fr/Fs61	60	1.17	Class 1
NFs8	59, 60	1.43	Class 1	Fr/Fs62	-	-	-
NFs9	26	1.19	Class 1	Fr/Fs63	38, 61, 62	1.03	Class 1
NFs10	27	1.14	Class 1	Fr/Fs64	38, 61	1.93	Class 2
NFs11	27	1.27	Class 1	Fr/Fs65	37	1.23	Class 1
NFs12	27	1.75	Class 2	Fr/Fs66	18	1.29	Class 1
SSFs13	4, 5	0.98	Class 1	Fr/Fs67	-	-	-
SSFs14	20, 37	1.05	Class 1	Fr/Fs68	8, 9	1.07	Class 1
SSFs15	23, 24, 25	1.17	Class 1	Fr/Fs69	-	-	-

Table 1. Cont.

Mountain Front Segments	Catchments	S_{mf}	Class	Mountain Front Segments	Catchments	S_{mf}	Class
SSFs16	18	1.06	Class 1	Fr/Fs70	-	-	-
SSFs17	17, 37	1	Class 1	Fr/Fs71	9, 13, 14	1.17	Class 1
SSFs18	-	-	-	Fr/Fs72	9	1.17	Class 1
SSFs19	58	1.05	Class 1	Fr/Fs73	10, 11	1.28	Class 1
SSFs 20	59, 70	1.01	Class 1	Fr/Fs74	-	-	-
SSFs21	17, 37	0.73	Class 1	Fr/Fs75	8, 14	1.19	Class 1
SSFs22	60, 63	1.90	Class 2	Fr/Fs76	12, 14	1.29	Class 1
SSFs23	67	1.13	Class 1	Fr/Fs77	-	-	-
SSFs24	67	1.04	Class 1	Fr/Fs78	-	-	-
ThFs25	11, 12	2.0	Class 2	Fr/Fs79	-	-	-
ThFs26	13, 14	1.87	Class 2	Fr/Fs80	44	1.33	Class 1
ThFs27	18, 19	1.01	Class 1	Fr/Fs81	-	-	-
ThFs28	18, 19	1.15	Class 1	Fr/Fs82	-	-	-
ThFs29	6, 19, 22	1.3	Class 1	Fr/Fs83	-	-	-
ThFs30	18, 20, 23	1.94	Class 2	Fr/Fs84	-	-	-
ThFs31	25	1.37	Class 1	Fr/Fs85	45, 46	1.28	Class 1
ThFs32	-	2.9	Class 3	Fr/Fs86	Fr/Fs75	-	-
ThFs33	1	1.71	Class 2	Fr/Fs87	Fr/Fs76	-	-
ThFs34	1, 3	1.84	Class 2	Fr/Fs88	Fr/Fs77	52	1.13
ThFs35	29, 30, 64	1.68	Class 2	Fr/Fs89	49, 51	1.27	Class 1
ThFs36	26, 27, 28, 65	1.93	Class 2	Fr/Fs90	47, 48		
Fr/Fs37	25, 26	1.25	Class 1	Fr/Fs91	47	1.09	Class 1
Fr/Fs38	3, 25	1.02	Class 1	Fr/Fs92	42, 43, 54	1.16	Class 1
Fr/Fs39	2	1.24	Class 1	Fr/Fs93	70	1.28	Class 1
Fr/Fs40	-	-	-	Fr/Fs94	-	-	-
Fr/Fs41	3	1.15	Class 1	Fr/Fs95	39	1.14	Class 1
Fr/Fs42	3	1.28	Class 1	Fr/Fs96	-	-	-
Fr/Fs43	-	-	-	Fr/Fs97	56	1.14	Class 1
Fr/Fs44	3	2.03	Class 2	Fr/Fs98	70	1.69	Class 2
Fr/Fs45	3, 22	1.17	Class 1	Fr/Fs99	70	1.23	Class 1
Fr/Fs46	3	1.30	Class 1	Fr/Fs100	70	1.11	Class 1
Fr/Fs47	3, 4	1.10	Class 1	Fr/Fs101	-	-	-
Fr/Fs48	-	-	-	Fr/Fs102	72	1.28	Class 1
Fr/Fs49	21, 22	1.62	Class 2	Fr/Fs103	71, 72	1.00	Class 1
Fr/Fs50	22, 23, 24	1.40	Class 1	Fr/Fs104	-	-	-
Fr/Fs51	27, 28, 65	1.42	Class 1	Fr/Fs105	72	0.97	Class 1
Fr/Fs52	31–35	1.50	Class 2	Fr/Fs106	-	-	-
Fr/Fs53	34, 62	2.26	Class 2	Fr/Fs107	69	1.23	Class 1
Fr/Fs54	-	-	-				

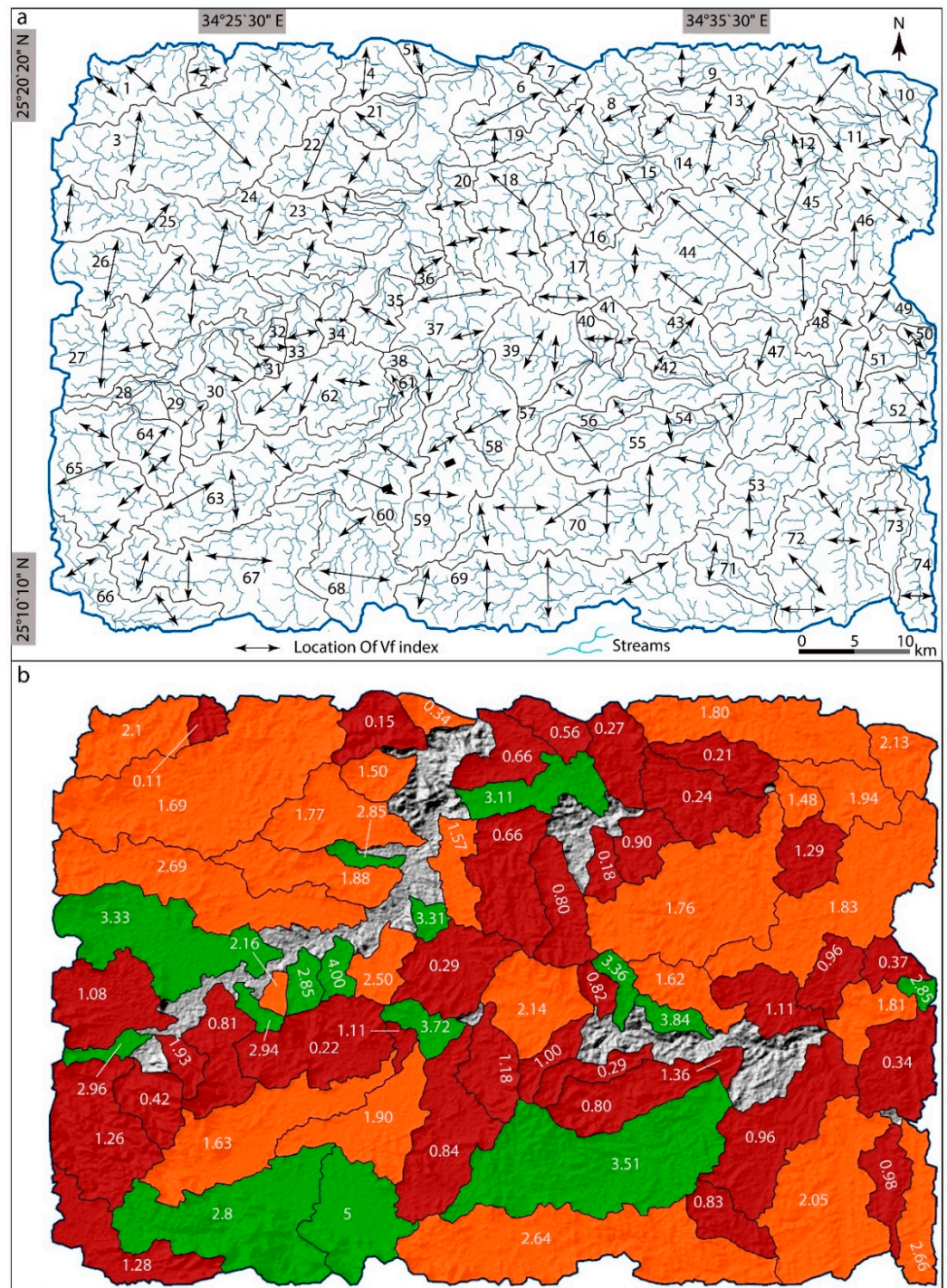


Figure 5. (a) Location of V_f calculation sections. Black numbers refer to the sub-catchment reference number. (b) Values and classes of V_f index for 74 identified sub-catchments. White numbers refer to the V_f values.

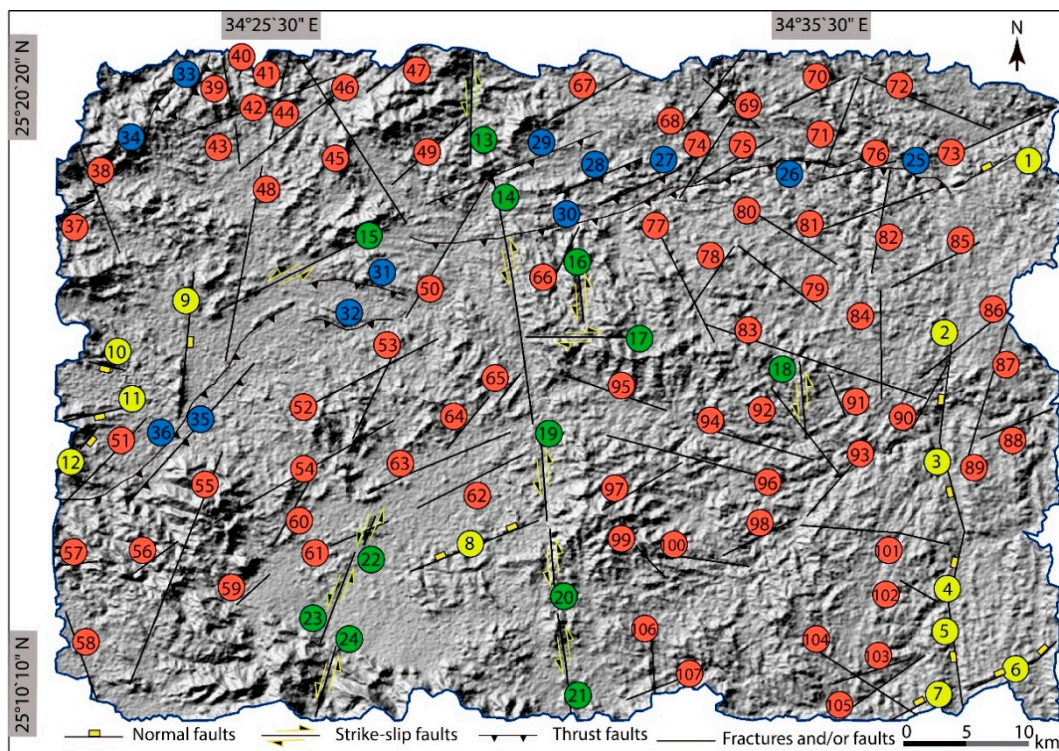


Figure 6. Locations and reference numbers of S_{mf} index for 107 identified mountain front segments. Mountain front sinuosity was calculated along every segment of the study area.

5.3. Asymmetry Factor Index (A_f)

The A_f index values show various basin asymmetry with block tilts. The values indicate that the symmetrical sub-catchments (Class 0) represent 24% of the total catchments of the studied sub-catchments (Figure 7). Class 1 sub-catchments are mostly located in the southern part of the study area and are represented by Sub-catchments 57, 60, 67, 69, and 70, while most of the north-western part of the study area is covered by Class 3 sub-catchments (Figure 7).

5.4. Drainage Basin Shape Index (B_s)

The B_s values are range from 0.56 (Sub-catchment 18) to 4.78 (Sub-catchment 69) (Figure 8). The active tectonic Class 2 occupies the majority of the study area by 40% of the total sub-catchments, while Class 1 is represented by only 17.5%. Similar to the results of the A_f index, most of the normal fault segments are marked by the lowest active tectonic B_s class (Figure 8).

5.5. Hypsometric Integral (H_i)

The H_i index values range from 0.20 (Sub-catchment 32) to 0.55 (Sub-catchment 45). In analyzing the H_i index map, one can infer that the majority of the study area is covered by H_i Class 2 (Figure 8). Class 1 sub-catchments are mostly located in the southern and western parts of the study area, while Class 2 is represented by the smallest area in the south-eastern part of the region (Figure 9).

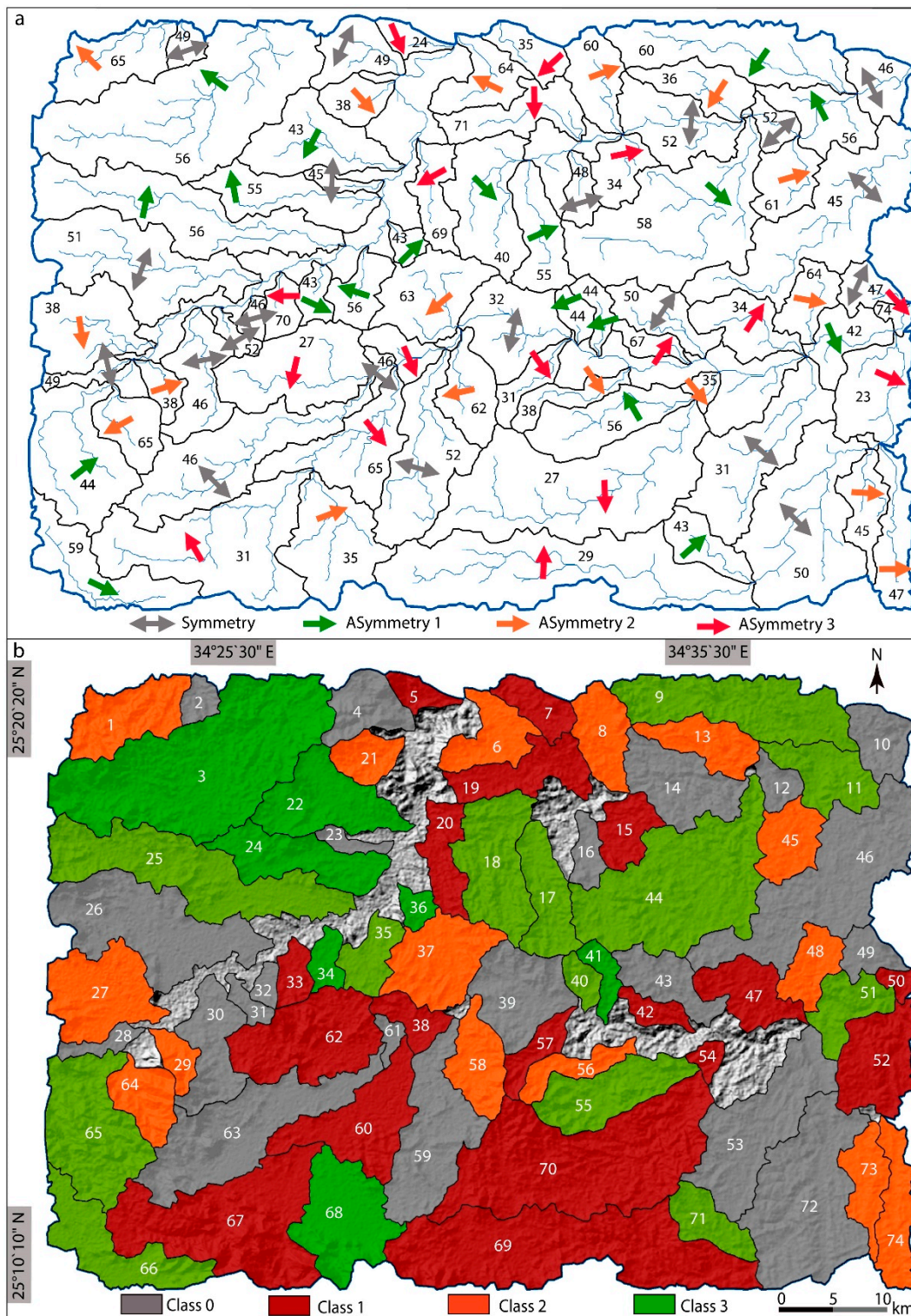


Figure 7. (a) Map illustrating tilting directions of sub-catchments. Black numbers refer to the A_f values. (b) Map showing classes of A_f index values. White numbers refer to the sub-catchment reference numbers.

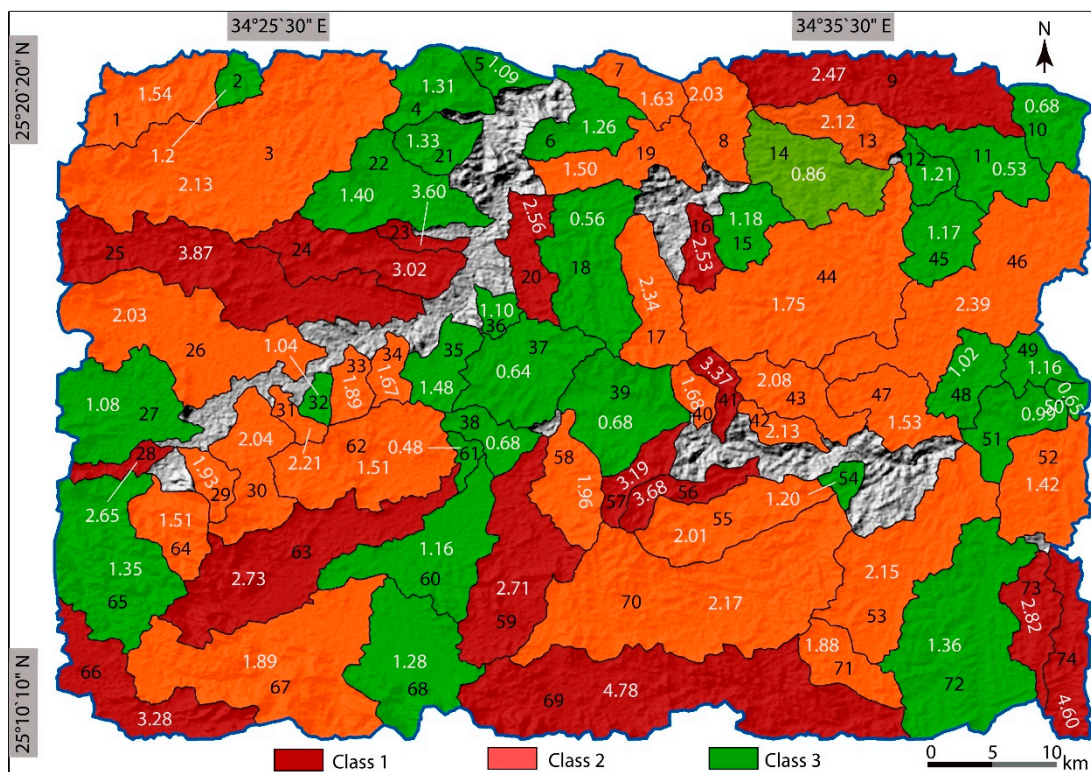


Figure 8. Map showing basin shape index (B_s) values in white numbers and tectonic classes. Black numbers refer to the sub-catchment reference numbers.

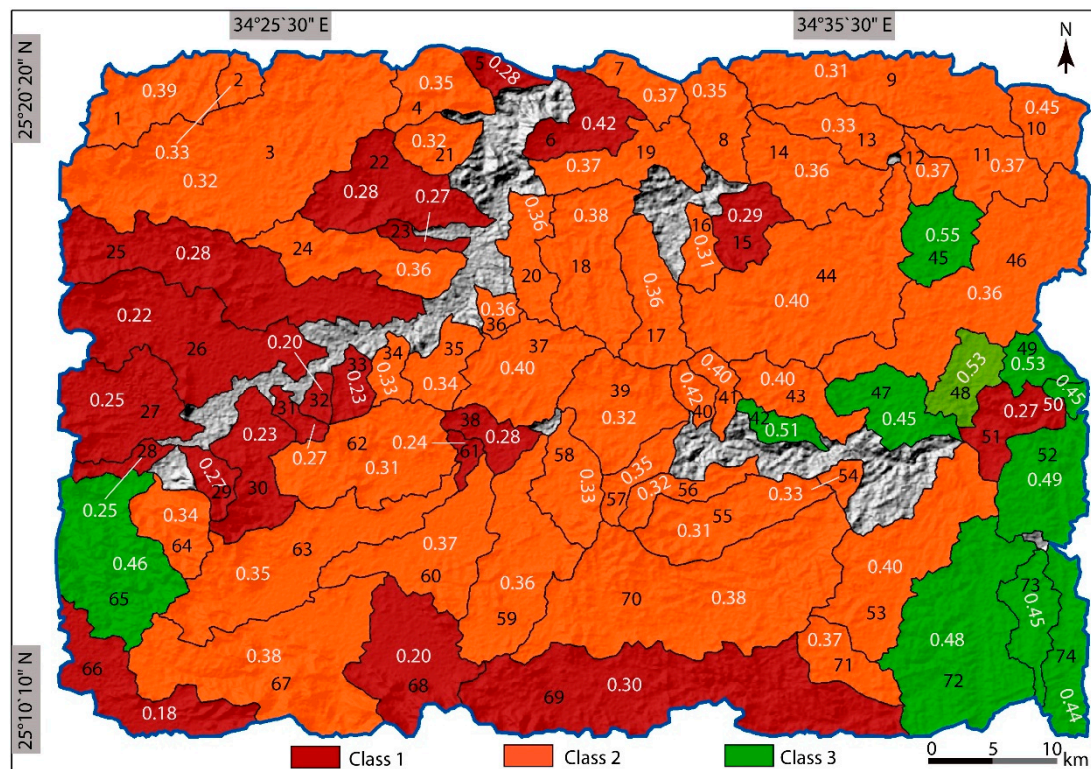


Figure 9. Map showing hypsometric integral index (H_i) values in white numbers and tectonic classes. Black numbers refer to the sub-catchment reference numbers.

5.6. Relative Tectonic Activity Index (RTAI)

A total of five morphological indexes were classified tectonically and averaged to define the RTAI (Table 2). According to the average values of the morphological indexes, the RTAI is grouped into three relative tectonic activity classes—(i) Class 1, high (<1.26); (ii) Class 2, moderate (1.26–1.73); (iii) Class 3, low (>1.73). The RTAI results show that Classes 2 and 3 cover most of the study area, while only 11% of the total sub-catchments distinguished by the RTAI represent Class 1 (Figure 10).

Table 2. Values and classes of morphological indexes and relative tectonic activity index (RTAI).

Catchment No.	V _f Class	S _{mf} Class	A _f Class	B _S Class	H _i Class	RTAI Value	RTAI Class
1	2	2	2	2	2	2	3
2	1	1	-	3	2	1.4	2
3	2	2	3	2	2	2	3
4	1	1	-	3	2	1.4	2
5	2	1	1	3	1	1.6	2
6	1	1	2	3	1	1.6	2
7	1	-	1	2	2	1.2	1
8	1	1	2	2	2	1.6	2
9	2	1	3	1	2	1.8	3
10	2	1	-	3	2	1.6	2
11	2	1	1	3	2	1.8	3
12	2	1	-	3	2	1.6	2
13	1	2	2	2	2	1.8	3
14	1	2	-	3	2	1.6	2
15	1	-	1	3	1	1.2	1
16	1	-	-	1	2	0.8	1
17	1	1	3	2	2	1.8	3
18	1	1	3	3	2	2	3
19	3	1	1	2	2	1.8	3
20	2	2	1	1	2	1.6	2
21	2	2	2	3	2	2.2	3
22	2	1	3	3	2	2.2	3
23	3	2	-	1	2	1.6	2
24	2	1	3	1	2	1.8	3
25	2	1	3	1	1	1.6	2
26	3	2	-	2	1	1.6	2
27	1	2	2	3	1	1.8	3
28	3	2	-	1	2	1.8	2
29	1	2	2	2	1	1.6	2
30	1	2	-	2	1	1.2	1
31	3	1	-	2	1	1.4	2
32	2	-	-	3	1	1.2	1
33	3	-	1	2	1	1.4	2
34	3	2	3	3	2	2.6	3

Table 2. Cont.

Catchment No.	V _f Class	S _{mf} Class	A _f Class	B _S Class	H _i Class	RTAI Value	RTAI Class
35	2	1	3	3	2	2.2	3
36	3	-	3	3	2	2.2	3
37	1	1	2	3	2	1.8	3
38	3	1	1	3	1	1.8	3
39	2	1	-	3	2	1.6	2
40	1	-	3	2	2	1.6	2
41	3	-	3	1	2	1.8	3
42	3	1	1	2	3	2	3
43	2	1	-	2	2	1.4	2
44	2	1	3	2	2	2	3
45	1	1	2	3	3	2	3
46	2	1	-	2	2	1.4	2
47	1	1	1	2	3	1.6	2
48	1	2	2	3	3	2.2	3
49	1	1	-	3	3	1.6	2
50	3	-	1	3	3	2	3
51	2	1	3	3	1	2	3
52	1	1	1	2	3	1.6	2
53	1	1	-	2	2	1.2	1
54	1	1	2	3	2	1.8	3
55	1	-	3	2	2	1.6	2
56	1	1	2	1	2	1.4	2
57	1	-	1	1	2	1	1
58	1	1	2	2	2	1.6	2
59	1	1	-	1	2	1	1
60	2	1	1	3	2	1.8	3
61	1	1	-	3	1	1.2	1
62	1	2	1	2	2	1.6	2
63	2	2	-	1	2	1.4	2
64	1	2	2	2	2	1.8	3
65	1	2	3	3	3	2.4	3
66	1	1	3	1	1	1.4	2
67	3	-	1	2	2	1.6	2
68	3	1	1	3	1	1.8	3
69	2	1	1	1	1	1.5	2
70	3	1	1	2	2	1.8	3
71	1	1	3	2	2	1.8	3
72	2	1	-	3	3	1.8	3
73	1	-	2	1	3	1.4	2
74	2	1	2	1	3	1.8	3

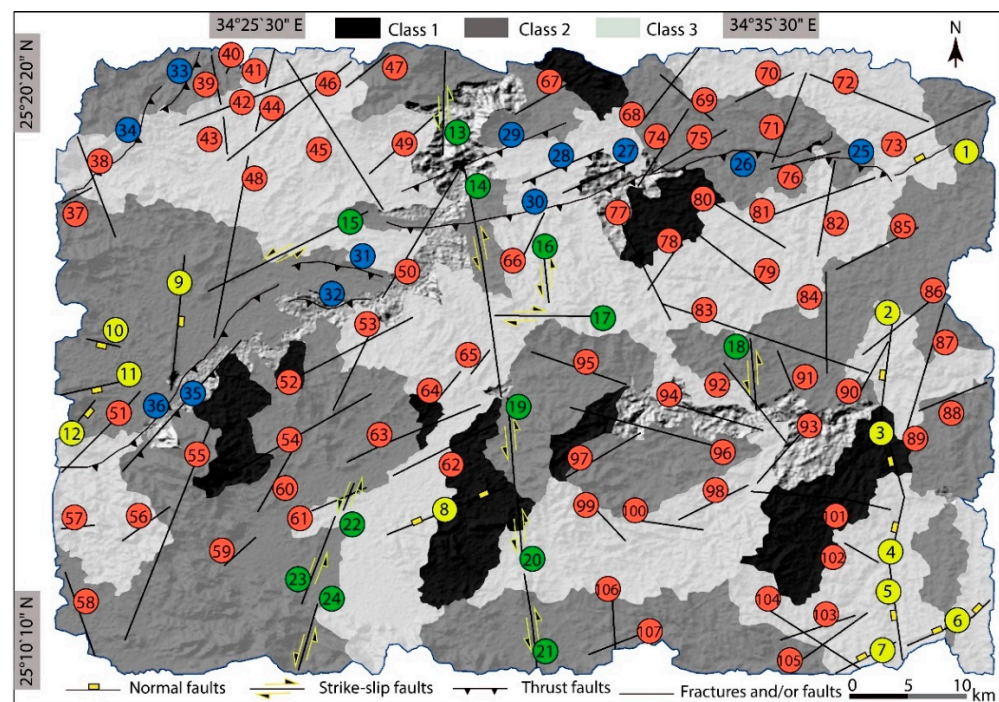


Figure 10. Map showing the distribution of the relative tectonic activity index (RTAI) of the study area.

6. Discussions on Relative Tectonic Activity

Active tectonic investigations using the relative tectonic activity index for active landforms and features have been performed by several researchers [5,6,55,56]. Many previous morphological studies have been carried out to evaluate the relative tectonic activity based on mountain fronts [1,5,7,57,58], which include the development of charts of the S_{mf} and V_f with reference values. In these previous studies, the researchers focused on the assessment of tectonic activity based on only the mountain fronts without evaluating the regional tectonic activity [55]. On the other hand, some used the average of the different indexes to categorize the tectonic activity into different classes, which was found to be more efficient for understanding the geomorphological evolution [6,32,33]. However, to date, such studies have not been performed in the Abu-Dabbab area until this present study.

Considering that the origin of seismicity (e.g., faulting or mantle-driven) of the Abu-Dabbab area is still under debate, investigating the tectonic activity and geomorphological properties contributes to our understanding of the controlling factors of this area's geomorphological evolution and seismicity. The researchers in ref. [26] stated that the Abu-Dabbab area is characterized by a small zone of earthquake hypocenters with a high degree of tectonic activity, while another study illustrated numerous earthquakes with small magnitudes ($<3.0 M_L$) [27]. Aiming to unravel the relationship between the seismic activity and geomorphological features, we attempted to evaluate the relative active tectonics of a large area (640 km^2) by quantifying five morphological indexes over 74 sub-catchments, including the V_f , S_{mf} , A_F , B_s , and H_i . This multiproxy analysis may reflect some results that depart markedly from the systematic outcomes. The authors in Refs. [55,56] considered these abnormal results as anomaly spots. Local uplifting and subsidence due to tectonic activity may reflect these anomalies, which have a range from weak to strong anomaly signatures.

6.1. Insights from the Morphological Indexes

We classified the RTAI into three class groups—(i) Class 1, which refers to high tectonic activity; (ii) Class 2, which refers to moderate tectonic activity; (iii) Class 3, which refers to the regions of low tectonic activity (e.g., S_{mf} index in Table 1; Figures 4 and 6–8). The distribution of these three RTAI classes is mapped in Figure 9 and listed in Table 2. We

evaluated our calculated morphological indexes along with the RTAI results for a collective interpretation.

The V_f values are used to distinguish, for example, V-shaped valleys and U-shaped valleys. While low V_f values point to V-shaped valleys and can be used to infer uplift-related active tectonics and incision, high values are related to U-shaped valleys, which might point to low relative tectonic activity or tectonic quiescence with weak marks of vertical uplift [2,56]. In the Abu-Dabbab area, low V_f values cover most of the region, pointing to possible tectonic activity and continuous deformation, whereas high V_f values that were computed for the southern part of the region indicate signatures of neotectonic movements (Figure 5). Low to moderate V_f values categorized within Class 1 of tectonic activity were calculated along the major strike-slip fault zone and in the southwestern part of the region, which hosts normal faults. Hence, we can infer that the Abu-Dabbab area has been undergoing fault-controlled valley development (Figure 5).

The mountain front sinuosity index (S_{mf}) is a proxy to investigate the tectonic uplift, which creates linearity along the mountain fronts, and river erosion, which causes irregular fronts [2,55]. Our results point to various S_{mf} values; nonetheless, the region is mainly represented by Classes 1 and 2 (Figure 6, Table 1) along thrust faults and faults and/or fractures, leading to low/medium asymmetry and, hence, a straight shape. On the other hand, the highest value, within Class 3, was computed for the northwestern part of the region, which might indicate erosional processes.

The A_f values, which are used to infer tectonic tilting based on basin asymmetry (low values indicate symmetry, high values indicate asymmetry) [59], show that Class 3 (high tectonic activity) sub-catchments are mainly localized in the northwest of the region (Figure 7). On the other hand, the southern part of the area is represented by Class 1 (low tectonic activity). The most remarkable conclusion that can be derived from this index is that most of the normal fault segments are covered by sub-catchments of very low tectonic activity. This finding is in agreement with the high V_f values that were calculated in the southern part of the Abu-Dabbab area and are possibly related to tectonic quiescence/low tectonic activity.

It is suggested that elongated drainage basin shapes are found in tectonically active areas and they tend to become circular as the tectonic activity decreases [42]. Accordingly, higher B_s values correspond to elongated basins and lower B_s values represent circular basins. Consequently, the majority of our B_s results (40%) are related to Class 2 of the RTAI, related to moderate activity, and only 17.5% of the B_s are related to Class 1 (high tectonic activity). Interestingly, the B_s values around the main strike-slip fault zone do not point to any prominent pattern that might relate to its activity (Figure 8).

The hypsometric integral (H_i) is a proxy for the elevation distribution of the study area where high values might point to young, uplifting, tectonic regions and low values indicate possibly eroded areas of low tectonic activity [55]. The Abu-Dabbab area is mainly represented by low values corresponding to tectonic activity Classes 1 and 2, which correspond to low and moderate tectonic activity, respectively. Along the major fault zone, similar to B_s values, an evident pattern is not observed (Figure 9).

The RTAI results show that the majority of the study area is controlled by low to medium tectonic activity, while the highest tectonic activities are represented by small spots that are recorded as separate sub-catchments. The RTAI analysis indicated that Class 1 comprises nine sub-catchments or 12% of the study area, Class 2 comprises 49 sub-catchments or 49%, and 39% of the study area is affected by Class 3 tectonic activity. Thus, around 88% of the studied sub-catchments are of low to moderate tectonic activity depending on the apparent morphological response. The normal fault segment 2 and strike-slip fault segment 15 are the only segments that are represented by the high tectonic activity class (Figure 10). This finding points to the swarming of micro-earthquakes rather than large magnitude earthquakes, supporting the results of the previous researchers [27,32]. Our study represents the most complete tectonic element dataset of the study area, combined with field evidence from various studies. Quantitative assessment applied here to

morphologic indexes, namely the valley shape (V_f), basin shape (B_S), basin asymmetry (A_f), mountain front sinuosity (S_{mf}), hypsometric integral (H_i), and subsequently, the computed RTAI results, point to the outcome that the high tectonic activity Class 1 covers only 12% of the region and the rest is represented by low to medium tectonic activity. Even though the major NFSZ is responsible for large magnitude earthquakes [27], one can infer that the NFSZ is accountable only for a small percentage of the tectonic activity but is not governing the landscape development of the Abu-Dabbab area. Consequently, we interpret that the geomorphology of the Abu-Dabbab area is not controlled by active faulting, for example, by the NFSZ primarily, but rather by faults and/or fractures that we have documented applying geospatial analysis (Figure 9). Indeed, the proposed method has been applied for morphotectonic analysis in Eastern Turkey, Spain, and the United States, with similar evidence of recent tectonic activity [1,5,6,50,52].

6.2. Origin of Seismicity

Uplift and vertical deformation rates of the active faults in the Abu-Dabbab area still do not give sufficient information about the Quaternary times. Hence, as an alternative approach, we applied tectonic geomorphology and geospatial analysis as techniques to investigate the tectonic activity over a large number of sub-catchments and aimed to detect even small clues that might suggest the origin of the seismicity.

In the study area, the detected tectonic elements are grouped into four categories—normal faults, strike-slip faults, thrust faults, and faults and/or fractures (Figures 2, 4b and 6). Normal faults trend N–S along the eastern part of the study area, with small segments trending in the NE–SW direction. Strike-slip faults mainly show NNW–SSE trend directions in five segments. Two NE–SW trending strike-slip faults were mapped, and only one segment trends in the E–W direction (Figure 6). The other faults and/or fractures are scattered in random directions all over the study area. The researchers in Ref. [26] have mapped low-angle active normal faults in several locations in the study area. The Abu-Dabbab area is mainly affected by the NFSZ and represents a complex set of sinistral strike-slip faults and a shear zone (NW–SE strike direction) [26]. Accordingly, the RTAI results related to the normal faults show that all normal faults crossing the study area show low to medium tectonic activity, except segments 2 and 7 (Figure 10). This implies that there are anomalies along most of the normal faults. Similarly, most of the strike-slip fault segments cross the areas of medium activity (segments 12, 13, 16, and 21). Segments 13, 15, 17, and 18 cross the areas of low tectonic activity, where only one segment (15) reflects the highest signals. Despite the strike-slip fault with a high relative tectonic activity segment, the RTAI map also shows anomalies along the strike-slip zones (Figure 8). Considering that the majority of the derived data (morphologic indexes) do not show any significant relationship with the main NFSZ, our results allow us to infer that the seismicity may not be related to the active faulting of the NFSZ primarily, but some other auxiliary processes might be causing the earthquake swarms in the Abu-Dabbab area. While high tectonic activity signals are few and distributed all over the study area instead of centralizing around the NFSZ, we can also infer from the RTAI results that there are tectonic anomalies along the major fault zone. Such localization of tectonic activities/anomalies, as we demonstrated in this study, is parallel to the findings of refs. [27,37]. Moreover, important tectonic proxies used in this study, such as B_S , V_f , and A_f , do not show any significant pattern along the NFSZ, further confirming this result. Accordingly, our study may potentially support previous authors who have discussed the mantle origin of the seismicity in the Abu-Dabbab area, relating it to the intrusion of upper-crust fluids in the structural zones [27]. A very recent study also revealed that important rare-metal deposits in the Abu-Dabbab area contain magmatic-hydrothermal fluid imprints [60]. In a neighboring locality (Quseir area) around 100 km to the north of the Abu-Dabbab region, a conceptual hydrothermal model was established based on subsurface structures [61]. It has been shown that the thermal waters are related to high heat flow. The author further suggested that geothermal potential is associated with deep fluid circulation within fault zones linked to the Red Sea rifting. In

addition to this, similar outcomes regarding the earthquake swarms were also suggested by other researchers who related the shallow depth (5–16 km), low-magnitude ($<5 M_L$) earthquake swarms to fluids and gasses that originate from magma around the East African Rift [62]. In fact, this assumption may not be an overinterpretation. Recent studies have shown that below the southern Red Sea, there is ongoing magmatic activity creating local earthquake swarms [63,64]. However, we would like to emphasize the need for further studies (e.g., tomographic imaging) to unequivocally infer the origin of seismicity in the Abu-Dabbab area.

7. Conclusions

In this study, we documented a complete dataset consisting of all mapped faults and fault/fracture elements of the study area. We examined the relative tectonic activity signals using ArcGIS, geospatial data, and five morphological indexes for the Abu-Dabbab region for the first time. Using the values of the valley floor width-to-valley floor height ratio (V_f), mountain front sinuosity (S_{mf}), asymmetry factor index (A_f), drainage basin shape index (B_s), and hypsometric integral (H_i), we classified every index into three tectonic activity classes. From these classes, we computed the average relative tectonic active index (RTAI) of all the indexes that divide the study area into three relative tectonic activity classes. According to the RTAI results, the high tectonic activities represent nearly one-tenth of the total sub-catchments of the study area in nine sub-catchments, while the rest of the area is divided between low and moderate tectonic activities. The medium tectonic activities recorded in this study confirm previous findings, which report low to medium magnitude earthquakes. Widely distributed tectonic activity classes indicate that the Abu-Dabbab landscape is not governed by the major Najd Fault Shear Zone but by the small fault and/or fracture structures. General morphological anomalies over the major faults and the localization of small magnitude tectonic activities identified in this study are suggestive of an auxiliary controlling factor (e.g., magmatic fluids) for earthquake swarming of the Abu-Dabbab region rather than the major Najd Fault Shear Zone. Future subsurface studies will immensely improve our knowledge of the geomorphological evolution of the Abu-Dabbab area and its relation to seismic activity.

Author Contributions: Conceptualization, Abdelrahman Khalifa; data acquisition, Abdelrahman Khalifa, Bashar Bashir, Abdullah Alsalman; methodology, Abdelrahman Khalifa and Bashar Bashir; software, Abdelrahman Khalifa and Abdullah Alsalman; validation, Abdelrahman Khalifa, Bashar Bashir, Abdullah Alsalman, and Nazik Öğretmen; formal analysis, Bashar Bashir, Abdullah Alsalman; investigation, Abdelrahman Khalifa and Nazik Öğretmen; resources, Nazik Öğretmen; data curation, Abdelrahman Khalifa and Bashar Bashir; writing—original draft preparation, Abdelrahman Khalifa; writing—review and editing, Abdullah Alsalman, and Nazik Öğretmen; visualization, Abdelrahman Khalifa; project administration, Bashar Bashir and Abdullah Alsalman. All authors have read and agreed to the published version of the manuscript.

Funding: This research was funded by the RESEARCHERS SUPPORTING PROJECT, grant number RSP-2021/296, King Saud University, Riyadh, Saudi Arabia.

Institutional Review Board Statement: Not applicable.

Informed Consent Statement: Not applicable.

Data Availability Statement: Not applicable.

Acknowledgments: The authors are grateful to the editor P. Blišťan for the editorial handling of the manuscript. The authors also thank the three anonymous reviewers; their comments and recommendations helped us improve the manuscript.

Conflicts of Interest: The authors declare no conflict of interest.

References

1. Yıldırım, C. Relative tectonic activity assessment of the Tuz Gölü Fault zone; Central Anatolia, Turkey. *Tectonophysics* **2014**, *630*, 183–192. [[CrossRef](#)]
2. Buczek, K.; Górnik, M. Evaluation of tectonic activity using morphometric indices: Case study of the Tatra Mts. (Western Carpathians, Poland). *Environ. Earth Sci.* **2020**, *79*, 176. [[CrossRef](#)]
3. Cosentino, D.; Schildgen, T.F.; Cipollari, P.; Faranda, C.; Gliozzi, E.; Hudáčková, N.; Lucifora, S.; Strecker, M.R. Late Miocene surface uplift of the southern margin of the Central Anatolian Plateau, Central Taurides, Turkey. *GSA Bull.* **2012**, *124*, 133–145. [[CrossRef](#)]
4. Moucha, R.; Forte, A.M.; Rowley, D.B.; Mitrovica, J.X.; Simmons, N.A.; Grand, S.P. Deep mantle forces and uplift of the Colorado Plateau. *Geophys. Res. Lett.* **2009**, *36*, 1–6. [[CrossRef](#)]
5. D'Agostino, N.; Jackson, J.A.; Dramis, F.; Funiciello, R. Interaction between mantle upwelling, drainage evolution and active normal faulting: An example from the central Apennines (Italy). *Geophys. J. Int.* **2001**, *147*, 475–497. [[CrossRef](#)]
6. Khalifa, A.; Çakir, Z.; Kaya, Ş.; Gabr, S. ASTER spectral band ratios for lithological mapping: A case study for measuring geological offset along the Ermenek segment of the East Anatolian Fault Zone, Turkey. *Arab. J. Geosci.* **2020**, *13*, 1–8. [[CrossRef](#)]
7. Gao, M.; Chen, G.; Xu, X. Geomorphic indices indicated recent differential tectonic uplift of the Lintan-Dangchang fault and the Minxian-Zhangxian earthquake. *Seism. Geol.* **2015**, *37*, 709–718.
8. Bali, B.S.; Wani, A.A.; Khan, R.A.; Ahmed, S. Morphotectonic analysis of the Madhumati watershed, northeast Kashmir valley. *Arab. J. Geosci.* **2016**, *9*, 1–17. [[CrossRef](#)]
9. Chandniha, S.K.; Kansal, M.L. Prioritization of sub-watersheds based on morphometric analysis using geospatial technique in Piperiya watershed, India. *Appl. Water Sci.* **2017**, *1*, 329–338. [[CrossRef](#)]
10. Khalifa, A.; Çakir, Z.; Owen, L.; Kaya, Ş. Morphometric Analysis of the East Anatolian Fault, Turkey. *Turk. J. Earth Sci.* **2018**, *27*, 110–126.
11. Khalifa, A.; Çakir, Z.; Owen, L.; Kaya, Ş. Evaluation of the Relative Tectonic Activity of the Adiyaman fault within the Arabian-Anatolian plate boundary (eastern Turkey). *Geol. Acta* **2019**, *6*, 1–17.
12. Baruah, M.P.; Bezbaruah, D.; Goswami, T.K. Active tectonics deduced from geomorphic indices and its implication on economic development of water resources in South-Eastern part of Mikir massif, Assam, India. *Geol. Ecol. Landsc.* **2020**, 1–14. [[CrossRef](#)]
13. Paichoon, M.S. Tectonic Geomorphology and Quaternary evolution of playas: A case study of Ernan Playa, central Iran. *Arab. J. Geosci.* **2021**, *14*, 1–18.
14. Armitage, J.J.; Duller, R.A.; Whittaker, A.C.; Allen, P.A. Transformation of tectonic and climatic signals from source to sedimentary archive. *Nat. Geosci.* **2011**, *4*, 231–235. [[CrossRef](#)]
15. Guarnieri, P.; Pirrotta, C. The response of drainage basins to the late quaternary tectonics in the Sicilian side of the Messina strait (NE Sicily). *Geomorphology* **2008**, *95*, 260–273. [[CrossRef](#)]
16. Zhang, T.; Fan, S.; Chen, S.; Li, S.; Lu, Y. Geomorphic evolution and neotectonics of the Qianhe River Basin on the southwest margin of the Ordos Block, north China. *J. Asian Earth Sci.* **2018**, *176*, 184–195. [[CrossRef](#)]
17. Bishop, P. Long-term landscape evolution: Linking tectonics and surface processes. *Earth Surf. Process. Landf.* **2007**, *32*, 329–365. [[CrossRef](#)]
18. Demoulin, A.; Beckers, A.; Hubert-Ferrari, A. Patterns of Quaternary uplift of the Corinth rift southern border (N Peloponnese, Greece) revealed by fluvial landscape morphometry. *Geomorphology* **2015**, *246*, 188–204. [[CrossRef](#)]
19. Dehbozorgi, M.; Pourkermani, M.; Arian, M.; Matkan, A.A.; Hosseiniasl, A. Quantitative analysis of relative tectonic activity in the Sarvestan area, Central Zagros, Iran. *Geomorphology* **2010**, *121*, 329–341. [[CrossRef](#)]
20. Matoš, B.; Pérez-Peña, J.V.; Tomljenović, B. Landscape response to recent tectonic deformation in the SW Pannonian Basin: Evidence from DEM-based morphometric analysis of the Bilogora Mt. area, NE Croatia. *Geomorphology* **2016**, *263*, 132–155. [[CrossRef](#)]
21. Daradich, A.; Mitrovica, J.X.; Pysklywec, R.; Willett, S.; Marco Forte, A. Mantle flow, dynamic topography, and rift-flank uplift of Arabia. *Geology* **2003**, *31*, 901–904. [[CrossRef](#)]
22. Faccenna, C.; Glišović, P.; Forte, A.; Becker, T.W.; Garzanti, E.; Sembroni, A.; Gvirtzman, Z. Role of dynamic topography in sustaining the Nile River over 30 million years. *Nat. Geosci.* **2019**, *12*, 1012–1017. [[CrossRef](#)]
23. Pik, R.; Marty, B.; Carignan, J.; Lavé, J. Stability of the Upper Nile drainage network (Ethiopia) deduced from (U-Th)/He thermochronometry: Implications for uplift and erosion of the Afar plume dome. *Earth Planet. Sci. Lett.* **2003**, *215*, 73–88. [[CrossRef](#)]
24. ArRajehi, A.; McClusky, S.; Reilinger, R.; Daoud, M.; Alchalbi, A.; Ergintav, S.; Gomez, F.; Shloan, J.; Bou-Rabee, F.; Ogubazghi, G.; et al. Geodetic constraints on present-day motion of the Arabian plate: Implications for Red Sea and Gulf of Aden rifting. *Tectonics* **2010**, *29*, 1–10. [[CrossRef](#)]
25. McKenzie, D.P.; Davies, D.; Molnar, P. Plate tectonics of the Red Sea and East Africa. *Nature* **1970**, *226*, 243–248. [[CrossRef](#)]
26. Hamimi, Z.; Hagga, W. A new tectonic model for Abu-Dabbab seismogenic zone (Eastern Desert, Egypt): Evidence from field-structural, EMR and seismic data. *Arab. J. Geosci.* **2016**, *10*, 1–11. [[CrossRef](#)]
27. Mohamed, A.S.; Hosny, A.; Abou-Aly, N.; Saleh, M.; Rayan, A. Preliminarily crustal deformation model deduced from GPS and earthquakes' data at Abu-Dabbab area, eastern desert, Egypt. *NRIAG J. Astron. Geophys.* **2013**, *2*, 67–76. [[CrossRef](#)]

28. Hosny, A.; El-Hady, S.M.; Guidarelli, M.; Panza, G.F. Source moment tensors of the earthquake swarm in Abu Dabbab area. South-East Egypt. *Rend. Lincei Sci. Fis. Nat.* **2012**, *23*, 149–163.
29. Azza, M.; Hosny, A.; Gharib, A. Rupture process of shallow earthquakes of Abou-Dabbab area, southeast of Egypt. *Egypt J. Appl. Geophys.* **2012**, *11*, 85–100.
30. Basheer, A.A.; Toni, M.; Abdelmotaal, A.M.; Omar, K. Using the HEM technique and its relation to the seismic activity to detect the main structural setting and rock units at Abu-Dabbab area. *Egypt Br. J. Appl. Sci. Technol.* **2015**, *9*, 327–337. [[CrossRef](#)]
31. El Khrepy, S.; Koullakov, I.; Al-Arifi, N. Crustal structure in the area of the Canoon earthquakes of Abu Dabbab (Northern Red Sea, Egypt), From seismic Tomography inversion. *Bull. Seismol. Soc. Am.* **2015**, *105*, 1–13. [[CrossRef](#)]
32. Morgan, P.; Keller, G.R.; Boulos, F.K. Earthquake cannons in the Egyptian Eastern Desert. *Bull. Seismol. Soc. Am.* **1981**, *71*, 551–554. [[CrossRef](#)]
33. Ibrahim, M.E.; Yokoyama, I. Probable origin of the Abu Dabbab earthquakes swarms in the Eastern Desert of Egypt. *Bull. Seismol. Soc. Am.* **1998**, *71*, 32.
34. Boulos, F.K. Some aspects of the geophysical regime of Egypt in relation to heat flow, groundwater and microearthquakes. In *Geology of Egypt*; Said, R., Ed.; Balkema: Rotterdam, The Netherlands, 1990; pp. 99–108.
35. Sami, M.; Hassoup, A.; Hosny, A.; Mohamed, G.A. Seismicity, arrival time delays of the seismic phases and slowness characteristics study in Abu Dabbab area, Egypt. *NRIAG J. Astron. Geophys.* **2013**, *2*, 234–242. [[CrossRef](#)]
36. Ögretmen, N.; Cipollari, P.; Frezza, V.; Faranda, C.; Karanika, K.; Gliozzi, E.; Radeff, G.; Cosentino, D. Evidence for 1.5 km of uplift of the Central Anatolian Plateau's southern margin in the last 450 kyr and implications for its multi-phased uplift history. *Tectonics* **2018**, *37*, 359–390. [[CrossRef](#)]
37. Schildgen, T.F.; Cosentino, D.; Bookhagen, B.; Niedermann, S.; Yıldırım, C.; Echtler, H.; Wittmann, H.; Strecker, M.R. Multi-phased uplift of the southern margin of the Central Anatolian plateau, Turkey: A record of tectonic and upper mantle processes. *Earth Planet. Sci. Lett.* **2012**, *317*, 85–95. [[CrossRef](#)]
38. Racano, S.; Jara-Muñoz, J.; Cosentino, D.; Melnick, D. Variable Quaternary Uplift Along the Southern Margin of the Central Anatolian Plateau Inferred From Modeling Marine Terrace Sequences. *Tectonics* **2020**, *39*, 5921. [[CrossRef](#)]
39. Rudge, J.F.; Roberts, G.G.; White, N.J.; Richardson, C.N. Uplift histories of Africa and Australia from linear inverse modelling of drainage inventories. *J. Geophys. Res. F Earth Surf.* **2015**, *120*, 894–914. [[CrossRef](#)]
40. Roberts, G.G.; White, N.J.; Martin-Brandis, G.L.; Crosby, A.G. An uplift history of the Colorado Plateau and its surroundings from inverse modelling of longitudinal river profiles. *Tectonics* **2012**, *31*, 1–25. [[CrossRef](#)]
41. Hussein, H.M.; Moustafa, S.S.R.; Elawadi, E.; Al-Arifi, N.S. Seismological Aspects of the Abou Dabbab region, Eastern Desert, Egypt. *Seismol. Res. Lett.* **2011**, *82*, 81–88. [[CrossRef](#)]
42. Shalaby, A.; Stüwe, K.; Makroum, F.; Fritz, H.; Kebede, T.; Klotzli, U. The Wadi Mubatek belt, Eastern Desert of Egypt: A Neoproterozoic conjugate shear system in the Arabian-Nubian shield. *Precambrian Res.* **2005**, *136*, 27–50. [[CrossRef](#)]
43. Stern, R.J. Arc Assembly and continental collision in the Neoproterozoic East African orogeny: Implication for the consolidation of Gondwanaland. *Annu. Rev. Earth Planet. Sci.* **1994**, *22*, 319–351. [[CrossRef](#)]
44. Youssef, M.I. Structural pattern of Egypt and its interpretation. *Bull. Am. Assoc. Pet. Geol.* **1982**, *53*, 601–614.
45. Conoco and General Petroleum Corporation. *Geological Map of Egypt, Scale 1:500,000*; Gebel Hamata: Cairo, Egypt, 1987.
46. Daggett, P.H.; Morgan, P.; Boulos, F.K.; Hennin, S.F.; El-Sherif, A.A.; Melek, Y.S. Microearthquake studies of the northeastern margin of the African Plate. *Ann. Geol. Surv. Egypt* **1980**, *10*, 989–996.
47. Daggett, P.H.; Morgan, P.; Boulos, F.K.; Hennin, S.F.; El-Sherif, A.A.; ElSayed, A.A.; Basta, N.Z.; Melek, Y.S. Seismicity and active tectonics of the Egyptian Red Sea margin and the northern Red Sea. *Tectonophysics* **1986**, *125*, 313–324. [[CrossRef](#)]
48. Mohamed, A.S.; Saleh, M.; Mahmoud, S.; Teleab, A.; Othman, A.A.; Hamed, D. Recent crustal deformation and seismicity studies at Abu-Dabbab area, Red Sea, Egypt. *Arab. J. Geosci.* **2013**, *6*, 1283–1293. [[CrossRef](#)]
49. Strahler, A.N. Hypsometric (area-altitude) analysis of erosional topography. *Geol. Soc. Am. Bull.* **1952**, *63*, 1117–1142. [[CrossRef](#)]
50. Keller, E.A.; Pinter, N. *Active Tectonics: Earthquakes, Uplift and Landscapes*, 2nd ed.; Prentice Hall: Upper Saddle River, NJ, USA, 2002.
51. Silva, P.G.; Goy, J.F.; Zazo, C.; Bardajm, T. Fault generated mountain fronts in Southeast Spain: Geomorphologic assessment of tectonic and earthquake activity. *Geomorphology* **2008**, *250*, 203–226. [[CrossRef](#)]
52. Bull, W.B.; McFadden, L.D. Tectonic geomorphology north and south of the Garlock fault, California. In *Geomorphology in Arid Regions, Proceedings of the Eighth Annual Geomorphology Symposium, Binghamton, NY, USA, 23–24 September 1977*; Doehring, D.O., Ed.; State University of New York: Albany, NY, USA, 1977; pp. 115–138.
53. Mayer, L. *Introduction to Quantitative Geomorphology*; Prentice Hall: Englewood, NJ, USA, 1990.
54. Hack, J.T. Stream-profiles analysis and stream-gradient index. *J. Res. U.S. Geol. Surv.* **1973**, *1*, 421–429.
55. El Hamdouni, R.; Irigaray, C.; Fernandez, T.; Chacon, J.; Keller, E.A. Assessment of relative active tectonics, southwest border of Sierra Nevada (Southern Spain). *Geomorphology* **2008**, *96*, 150–173. [[CrossRef](#)]
56. Mahmood, S.A.; Gloaguen, R. Appraisal of active tectonics in Hindu Kush: Insights from DEM derived geomorphic indices and drainage analysis. *Geosci. Front.* **2012**, *3*, 407–428. [[CrossRef](#)]
57. Azor, A.; Keller, E.A.; Yeats, R.S. Geomorphic indicators of active fold growth: Oak Ridge anticline, Ventura basin, southern California. *GSA Bull.* **2002**, *114*, 745–753. [[CrossRef](#)]

58. Rockwell, T.K.; Keller, E.A.; Johnson, D.L. Tectonic geomorphology of alluvial fans and mountain fronts near Ventura, California. In *Tectonic Geomorphology, Proceedings of the 15th Annual Geomorphology Symposium*; Morisawa, M., Ed.; Allen and Unwin Publishers: Boston, MA, USA, 1985; pp. 183–207.
59. Pérez-Peña, J.V.; Azor, A.; Azañón, J.M.; Keller, E.A. Active tectonics in the Sierra Nevada (Betic Cordillera, SE Spain): Insights from geomorphic indexes and drainage pattern analysis. *Geomorphology* **2010**, *119*, 74–84. [[CrossRef](#)]
60. Zoheir, B.; Lehmann, B.; Emam, A.; Radwan, A.; Zhang, R.; Bain, W.M.; Steele-MacInnis, M.; Nolte, N. Extreme fractionations and magmatic-hydrothermal transition in the formation of Abu Dabbab rare-metal granite, Eastern Desert, Egypt. *Lithos* **2020**, *352–353*, 105329. [[CrossRef](#)]
61. Mohamed, H.S. Subsurface structures and conceptual hydrothermal model of the area lying between Quseir and Safaga area, Red Sea Coast, Egypt. *Arab. J. Geosci.* **2021**, *14*, 49. [[CrossRef](#)]
62. Lindenfeld, M.; Rumpker, G.; Batte, A.; Schumann, A. Seismicity at the Rwenzori Mountains, East African Rift: Earthquakes distribution, magnitudes and source mechanisms. *Solid Earth Discuss.* **2012**, *4*, 565–598.
63. Xue, L.; Alemu, T.; Gani, N.D.; Abdelsalam, M.G. Spatial and temporal variation of tectonic uplift in the southern Ethiopian Plateau from morphotectonic analysis. *Geomorphology* **2018**, *309*, 98–111. [[CrossRef](#)]
64. Ruch, J.; Keir, D.; Passaelli, L.; Di Giacomo, D.; Ogubazghi, G.; Jónsson, S. Revealing 60 years of Earthquake Swarms in the Southern Red Sea, Afar and the Gulf of Aden. *Front. Earth Sci.* **2021**, *9*, 1–20. [[CrossRef](#)]